

Pressure-Induced Volume Collapse and Metallization in Inverse Spinel Co_2TiO_4

Mrinmay Sahu,^{1,2} Souvick Chakraborty,¹ Bidisha Mukherjee,^{1,2} Bishnupada Ghosh,³
Asish Kumar Mishra,^{1,2} Satyabrata Raj,^{1,2} and Goutam Dev Mukherjee^{1,2,*}

¹*Department of Physical Sciences, Indian Institute
of Science Education and Research Kolkata,
Mohanpur, Nadia, West Bengal-741246, India*

²*National Centre for High Pressure Studies,
Indian Institute of Science Education and Research Kolkata,
Mohanpur, Nadia, West Bengal-741246, India*

³*Diamond Light Source Ltd, Harwell Science and Innovation Campus,
Didcot OX11 0DE, United Kingdom*

(Dated: April 8, 2025)

Abstract

The structural, vibrational, electronic, and magnetic properties of inverse spinel Co_2TiO_4 (CTO-Sp) under high pressure (HP) conditions are systematically investigated using X-ray diffraction, Raman spectroscopy, in situ optical microscopy, and first-principles density functional theory (DFT) calculations. At ambient conditions, CTO-Sp exhibits a cubic phase with a space group $Fd\bar{3}m$, and it undergoes two notable structural phase transitions at HP. The first transition, occurring at approximately 7.2 GPa, leads to the tetragonal- $I4_1/amd$ phase with minimal alteration in unit cell volume. Subsequently, a second transition to an orthorhombic phase with a mixed space group $Fddd$ and $Cmcm$ is observed around 17.3 GPa. This second structural transition corresponds to a first-order phase transition involving a significant reduction in unit cell volume of approximately 17.5%. The bulk compressibility of CTO-Sp and its HP post-spinel phases is almost equal to the average polyhedral compressibility within each phase. DFT calculations reveal a high-spin to low-spin transition, accompanied by the collapse of local magnetic moments in the $Cmcm$ orthorhombic phase, leading to the sample's pressure-induced metallization.

I. INTRODUCTION

Binary and ternary spinels have attracted significant attention, not solely owing to their distinctive physical properties, including multiferroicity, unconventional magnetic behaviour, negative thermal expansion, and magnetodielectric effects, but also due to their diverse range of applications in high-frequency electronic components, sensors, and ultrahigh-density magnetic recording media [1–8]. Spinel oxides follow the general formula AB_2O_4 , where A and B represent transition metal ions. Based on the distribution of cations, spinels are categorized into two types: normal spinel, characterized by the formula $[A^{2+}]_T[(B^{3+})_2]_oO_4$, and inverse spinel, identified by the formula $[B^{3+}]_T[(A^{2+}B^{3+})]_oO_4$. In the normal spinel, $[A^{2+}]_T$ occupies the tetrahedral site, while two $[B^{3+}]_o$ cations occupy octahedral sites. This arrangement differs from the inverse spinel, where $[B^{3+}]_T$ cations are in tetrahedral sites, and $[A^{2+}B^{3+}]_o$ cations are in octahedral sites within a single formula unit. In an inverse spinel structure, 50% of the octahedral sites are occupied by A cations, while B cations are distributed between both octahedral and tetrahedral sites [19]. At ambient conditions, the majority of

* Corresponding Author: goutamdev@iiserkol.ac.in

spinel cobaltites and ferrites crystallize into normal cubic symmetry, but this configuration becomes unstable under high pressure (HP), as well as at elevated temperatures [10, 11]. Increasing pressure or temperature induces disorder in the tetrahedral [A] and octahedral [B] sites, subsequently adjusting the Curie temperature of the magnetic spinel and triggering a magnetic transition [12–14]. Normal and inverse spinels exhibit a range of structural phase transitions under pressure, leading to the formation of various polymorphs. Within their pressure/temperature-induced post-spinel phases and diverse polymorphic forms, numerous intriguing properties have been discovered. These include electronic characteristics such as insulator-to-metal transitions (IMTs), superconductivity, spin reorientation linked to magnetic transitions, Mott transitions, high spin to low spin transitions, and colossal magnetoresistance. These phenomena arise from the delicate interplay between crystal lattice distance and electronic degrees of freedom. The thermodynamic properties of numerous spinels can also be externally adjusted through perturbations, such as changes in pressure and temperature [11, 15, 17].

In the field of Earth sciences, there has been significant interest in the pressure-induced phase transformations of titanate spinels (A_2TiO_4 -Sp; where A can be any transition metal). These spinels have captured attention due to their conventional classification as low-pressure analogs of ringwoodite, the most abundant mineral in the lower section of the mantle transition zone. Therefore, the exploration of the HP behaviour of the inverse spinel, Co_2TiO_4 (CTO-Sp), is anticipated to provide crucial insights into understanding the dynamics of Earth’s lower mantle [18–22]. Cobalt orthotitanate, CTO-Sp, typically adopts the cubic crystal structure with the space group $Fd\bar{3}m$, and its electronic configuration is commonly assumed to be $(Co^{2+})_T(Co^{2+}Ti^{4+})_O O_4$, where the subscript T and O represent the tetrahedral and octahedral sites, respectively [23]. The findings revealed that CTO-Sp is a rare example exhibiting unusual semi spin glass (SSG) behaviour following a quasi-long-range ferrimagnetic ordering transition at $T_C = 48K$ and magnetic compensation behaviour at approximately $T_{comp} = 32K$, where the magnetizations of the two sublattices balance each other. Nevertheless, there remains a dispute regarding the existence of SSG state in CTO-Sp [23–26]. Random anisotropy is a key factor influencing the global behaviour of CTO-Sp. This anisotropy arises from unsystematic lattice distortion, which screens the local charge density fluctuation caused by the substantial charge difference between transition metal ions [27]. Pressure can induce lattice distortion and modify the shielding of local charge density

fluctuations, resulting in a modification of the global behaviour of CTO-Sp. Numerous experimental investigations utilizing various techniques have been undertaken to observe the HP post-spinel phase with varying polymorphs and to establish the equation of state for A_2TiO_4 spinels [18, 19, 28]. For instance, a Jahn-Teller transition from a cubic to a tetragonal structure at approximately 9 GPa has been documented in Fe_2TiO_4 . Additionally, an HP transition from the tetragonal to the orthorhombic structure of Fe_2TiO_4 has been identified at around 11 GPa, along with the discovery of a higher-pressure polymorph at approximately 45 GPa [29]. Theoretical simulations by Zhang et al. [30] indicate that CTO-Sp exhibits several post-spinel phases with various stable polymorphs in the HP range. They also predict a potential pressure-induced magnetic transition in the HP post-spinel phase. Unfortunately, there is a complete lack of HP data to validate the theoretical findings on CTO-Sp. Therefore, an HP investigation of CTO-Sp is highly desirable to comprehend post-spinel polymorphism, coupled with a potential pressure-induced magnetic transition associated with the Mott insulator-to-metal transition (MIT) [30].

In this study, we have synthesized polycrystalline CTO-Sp and investigated pressure-induced structural, vibrational and electronic properties, along with a potential magnetic transition, utilizing x-ray diffraction (XRD) and Raman spectroscopy, and first-principle density functional theory (DFT) calculations. Our HP XRD measurements up to 25.6 GPa reveal two structural phase transitions. The first is a cubic-to-tetragonal transition with a minimal unit cell volume change occurring around 7.2 GPa. The second phase transition involves a shift from the tetragonal phase to the orthorhombic phase with a mixed space group (Fddd and Cmcm), resulting in a significant unit cell volume collapse of approximately 17.5% in the Cmcm-orthorhombic phase at around 17.3 GPa. The proportion of the Cmcm-orthorhombic crystal structure increases with pressure, reaching its peak at the maximum pressure. Observations include a pressure-induced reduction of octahedral volume and an increase in octahedral distortion index beyond 17.3 GPa in the orthorhombic phase. Our HP Raman spectroscopy data support the cubic-to-tetragonal phase transition, as evidenced by a slope change in the E_g mode and the disappearance of the $T_{2g}(1)$ mode around 6.5 GPa. The emergence of a new peak and changes in the slope of $T_{2g}(2)$ and A_{1g} modes indicate a structural reorientation around 17.3 GPa, consistent with XRD measurements. DFT calculations show that a high-spin to low-spin transition occurs, causing the collapse of local magnetic moments in the Cmcm orthorhombic phase and leading to metallization under

pressure. The absence of certain Raman modes, along with the non-appearance of modes associated with the Cmc_m orthorhombic phase at high pressure, further supports the notion of a pressure-induced metallization.

II. EXPERIMENTAL DETAILS

The inverse spinel Co_2TiO_4 polycrystalline sample was synthesized via the conventional solid-state reaction route [31, 32]. A stoichiometric mixture of Co_3O_4 (99.9 % purity) and TiO_2 (99.5 % purity) powders, obtained from Sigma-Aldrich, was thoroughly blended using an agate mortar and pestle. The resulting mixture underwent calcination at 1100 °C for 24 hours to produce the pure CTO-Sp. The calcined powder was then compressed into pellet form under a hydrostatic pressure of 2.2 kbar, followed by sintering at 1200 °C for 20 hours in an air environment to achieve a high-density polycrystalline CTO-Sp sample. Subsequently, the sintered CTO-Sp pellet was crushed and grinded for a long time to obtain a fine powder, which was utilized for all experimental purposes. The phase purity of the polycrystalline CTO-Sp was verified using room temperature ambient pressure XRD measurements [31]. Energy Dispersive X-ray Spectroscopy (EDX) measurements were conducted to determine the average stoichiometric ratio of the sample. The grain size and distribution of the CTO-Sp powder were examined using Field Emission Scanning Electron Microscopy (FESEM). Detailed discussions on EDX data and FESEM data can be found in the supplemental information. We conducted room temperature ambient and HP x-ray diffraction measurements for CTO-Sp at the XPRESS beamline in the ELETTRA synchrotron radiation facility in Trieste, Italy, utilizing X-ray beam at the wavelength of 0.4957 Å. All HP experiments were carried out using a piston-cylinder type diamond anvil cell (DAC) from Almax easy Lab, with 300 μm dia diamond culets. A 290 μm thick steel gasket was pre-indented to a thickness of 40 μm using the DAC. This pre-indented steel gasket with a central hole of diameter 100 μm, was placed between two oppositely faced diamond anvils to create a suitable sample chamber. A minute amount of powder sample, approximately 50 μm in diameter, was loaded inside the sample chamber. Additionally, a small quantity of silver powder was mixed with the sample to serve as a pressure calibrant for HP XRD measurements. The 4:1 methanol-ethanol mixture was employed as a liquid pressure transmitting medium (PTM). The incident X-ray beam was collimated to a spot size diameter of 50 μm

and directed through the center of the gasket hole inside the DAC. The diffraction data were recorded using a PILATUS 3S 6M detector positioned perpendicular to the incident beam. The sample-to-detector distance was determined using the XRD patterns of the standard sample CeO_2 . DIOPTAS software was utilized to convert all 2D XRD images into 2θ vs intensity profiles [33]. The XRD patterns were indexed using CRYSFIRE software [34]. GSAS software was employed to conduct Le Bail and Rietveld refinements of the XRD patterns [35]. Raman spectra, both ambient and pressure-dependent, were acquired in the backscattering geometry using Monovista from SI GmbH, a confocal micro-Raman system consisting of a 750 mm monochromator and a back-illuminated PIXIS 100BR (1340×100) CCD camera. The sample was excited with the 532 nm laser from the Cobalt-samba diode pump laser source. To prevent local heating, the laser power was maintained at a constant level of approximately 20 mW. A 20X objective lens with infinite correction, offering a large working distance and a laser spot diameter of about 5 μm , was utilized for collecting the scattered radiation. A grating featuring 1500 grooves/mm was used to disperse the scattered light, achieving a spectral resolution better than 1.2 cm^{-1} . Throughout the entire experiment, the scattered signal collection area of the sample remained fixed. Ruby chips (approximate size 5-8 μm) were loaded alongside the powder sample in the sample chamber, serving as pressure markers during Raman spectroscopy measurements [36]. The ruby chips were positioned close to the sample. The sample loading technique inside the DAC was consistent with the description provided earlier. Similar to XRD, methanol-ethanol was utilized as a liquid PTM during HP Raman spectroscopy measurements. All experiments were conducted using the polycrystalline powders of Co_2TiO_4 sample.

III. COMPUTATIONAL DETAILS

Density Functional calculations were carried out using the Vienna Ab Initio Simulation Package (VASP) [37] with the generalized gradient approximation exchange-correlation functional in the form of the Perdew-Burke-Ernzerhof (GGA-PBE) [38]. The frozen-core Projector Augmented Wave (PAW) [39] technique with an energy cutoff of 500 eV for the plane wave basis was employed for the calculations. The lattice parameters were chosen from the experimental data for different values of pressures, whereas the ionic positions were allowed to relax to obtain the final structures. Each of the unit cells for the different

phases contains a different number of formula units and different lattice constants, and as such, the k -point grid is chosen in such a way that the product of the lattice constant and the number of k -points along any given direction is ~ 60 . For all the calculations, the energy convergence tolerance was set at 10^{-8} eV and the force tolerance for ionic optimization was kept at 10^{-3} eV/Å. The GGA+U method is used to treat the partially filled d orbitals of the Co atoms with $U_{eff} = 4.0$ eV kept fixed for all the phases.

IV. RESULTS AND DISCUSSION

A. High pressure x-ray powder diffraction

We have conducted HP X-ray powder diffraction measurements on CTO-Sp, covering the pressure range from ambient condition to 25.6 GPa, as illustrated in Figure 1. The reflection lines in the ambient XRD pattern were successfully indexed with the cubic phase, possessing the space group $Fd\bar{3}m$. The Rietveld analysis of the ambient XRPD pattern, depicted in Figure 2(a), confirms the stabilization of the cubic phase. Detailed information on the refined structural parameters is provided in Table I. The calculated unit cell parameters for the best fit are $a = b = c = 8.4473(7)\text{Å}$ with the corresponding unit cell volume, $V_0 = 602.788(13)\text{Å}^3$. Our data exhibits excellent agreement with the reported literature [31]. In the cubic phase, up to approximately 7.2 GPa, all the Bragg peaks are very sharp and well indexed with the space group $Fd\bar{3}m$. However, at and above 8.7 GPa, we observed broadening in some reflection lines. For our HP XRD measurements, we utilized a methanol-ethanol (4:1) mixture as a pressure-transmitting medium, which maintains hydrostatic conditions within the sample chamber up to 10 GPa [40?]. Therefore, the broadening of the reflection lines can not be attributed to the presence of any pressure gradient inside the DAC. The Bragg reflection line attributed to the Ag pressure marker remained sharp with a FWHM value of approximately $0.030(5)^\circ$ up to about 9.6 GPa. A careful inspection of the XRD pattern at 9.6 GPa showed splitting of the (4,0,0) Bragg peak of the cubic phase (Supplementary Fig.S3). A re-indexing of the XRD pattern at 9.6 GPa resulted in a tetragonal structure with corresponding $I4_1/amd$ crystal symmetry. The Rietveld analysis of the XRD pattern of CTO-Sp at 9.6 GPa, shown in Figure 2(b), indicates the stabilization of the tetragonal phase. The cell parameters for the best fit at 9.6 GPa are $a = b = 5.8845(7)\text{Å}$ and $c = 8.3374(5)$

\AA with the unit cell volume, $V_0 = 288.711(1) \text{\AA}^3$. The refined lattice parameters are very close to the unit cell parameters of the single-crystal Fe_2TiO_4 [29]. Detailed information regarding the refined structural parameters is provided in Table I. A Rietveld refinement of the XRD pattern at 8.7 GPa in the new tetragonal phase produced a better fit. In the cubic phase, the lattice parameter and unit cell volume exhibit a linear decrease with applied pressure up to approximately 7.2 GPa, as depicted in Figure 3(a) and Figure 4(a), respectively. Following the cubic to tetragonal phase transition around 8.7 GPa, a reduction in the lattice parameter "a" and an increase along the c-direction are observed (see Figure 3(a)). The tetragonality (c/a) of the unit cell in the tetragonal phase rises with pressure, reaching its maximum at 16.1 GPa, as illustrated in the inset of Figure 3(a). This increase in tetragonality typically signifies a transition to a lower symmetry structure. In Figure 1, at 17.3 GPa, a new diffraction peak at $2\theta = 10.7^\circ$ is observed, and another peak at $2\theta = 13.7^\circ$ begins to split at the same pressure. The intensity of the newly observed peak increases with pressure, reaching its maximum at the highest pressure of this study. At 19 GPa, a new broad peak around $2\theta = 16^\circ$ is observed, along with a peak splitting at $2\theta = 17.8^\circ$. Beyond 19 GPa, additional new diffraction peaks and peak splitting are observed (refer to Figure 1, where newly identified peaks are denoted by asterisks). All these newly observed peaks become more prominent under pressure, and the split peaks become more distinguishable with increasing pressure. Observing these new intense peaks and the splitting of diffraction peaks indicate a possible structural phase transition of CTO-Sp above 17 GPa. Interestingly, the XRD patterns could only be indexed to a mixed orthorhombic phase corresponding to space groups Fddd and Cmcm. In Figure 2(c), we have shown the Rietveld refinement analysis of the diffraction data at 19.1 GPa, which shows the excellent fit to the mixed orthorhombic phase in the space groups Fddd and Cmcm. The determined lattice parameters for the optimal fit of the XRD pattern at 19.1 GPa are as follows: (i) Fddd-orthorhombic: $a = 8.2650(2) \text{\AA}$, $b = 8.3321(7) \text{\AA}$, $c = 8.1670(6) \text{\AA}$, and $V_0 = 562.41(6) \text{\AA}^3$. (ii) Cmcm-orthorhombic: $a = 2.7521(7)$, $b = 8.8650(2)$, $c = 9.5185(8)$, and $V_0 = 232.220(4) \text{\AA}^3$. Detailed information regarding the refined structural parameters is presented in Table II. However, the phase fraction percentages for the Fddd and Cmcm space groups are 85.8 % and 14.2%, respectively, at 17.3 GPa.

Zhang et al. [30] reported a structural phase transition near 21 GPa, as evidenced by the appearance of new Bragg peaks, where the high-pressure XRD measurements were

carried out using Ne as a pressure-transmitting medium. Their decompression data show that at 1 atm, a broad and low-intensity Bragg peak (0 2 3) of the high-pressure phase remains, suggesting an almost reversible transition. The data published by Zhang et al. are insufficient to fully elucidate the nature of the post-spinel phases, as they provided very few data points beyond the phase transition. Additionally, they did not perform Rietveld refinement on their XRD data. In contrast, our Rietveld-refined XRD data provide evidence of a mixed-phase region above 17 GPa. Since Ne PTM remains hydrostatic till about 15 GPa, the difference in phase transition pressures possibly arises due to different pressure transmitting media used.

To assess the stability of the four distinct phases under different pressures - cubic ($Fd\bar{3}m$), tetragonal ($I4_1/amd$), and two orthorhombic phases ($Fddd$ and $Cmcm$) - first principle calculations were performed using the DFT + U formalism, with $U_{eff} = 4.0$ eV for the Co atoms. The optimized crystal structures for these phases are depicted in Figure 5. It is interesting to see the unit cell arrangement of inverse spinel CTO. Typically, in normal spinels with general formula AB_2O_4 , A^{2+} cations reside on the tetrahedral site (A site), while B^{3+} cations occupy the octahedral site (B site). However, in Co_2TiO_4 , cobalt exists single valence states, Co^{2+} [10]. Consequently, Co^{2+} occupies both the A and B sites in equal occupations, while the remaining 50% of the B site is filled by the Ti^{4+} ions. Hence, the formula for the inverse spinel CTO can be expressed as $Co(Co_{0.5}Ti_{0.5})_2O_4$. In the cubic, tetragonal, and $Fddd$ -orthorhombic phases, the unit cell of CTO-Sp is formed by a combination of $Co^{2+}O_4$ tetrahedra and $Co^{2+}/Ti^{4+}O_6$ octahedra. Conversely, in the case of $Cmcm$ space group, the unit cell is formed by a herringbone octahedral array. In this array, Co^{2+} occupies A site and Co^{2+}/Ti^{4+} are disorderly situated at B site. The arrangement of the cation-oxygen polyhedra for each phase is shown in Figure 5. The pressure-dependent phase fraction for the two different space groups in the orthorhombic phase is illustrated in Figure 3(b). Notably, the phase fraction for the $Cmcm$ space group increases with pressure, while the phase fraction for the $Fddd$ -orthorhombic phase decreases with pressure. At 17.3 GPa, the new diffraction peak at $2\theta = 10.7^\circ$ is responsible for the presence of the $Cmcm$ space group. The intensity of this new diffraction peak increases with rising pressure, directly correlating with the increase in the $Cmcm$ -phase fraction percentage. Conversely, all peaks responsible for the $Fddd$ space group gradually broaden under high pressure, which can be attributed to the decrease in the phase fraction percentage. At the highest pressure of around

25 GPa, the phase fraction for the Fddd and Cmc21 space groups is approximately 19 % and 81 %, respectively, as indicated in Figure 3(b). In the orthorhombic phase, within the Fddd space group, the c-axis displays greater compressibility compared to the other two axes. Conversely, in the Cmc21 space group, the compressibility of the b-axis is notably higher than that of the other two axes, see Figure 3(a). This directional variation in compression, known as anisotropic compression, implies that the bulk modulus can vary along distinct crystallographic directions in the post-spinel phase of CTO-Sp. Above 25 GPa, Rietveld refinement becomes challenging as the diffraction peak broadens with reduced intensity, hindering accurate analysis.

For the calculation of the isothermal bulk modulus (B_0) of CTO-Sp, we applied a least-squares method to fit the P-V data obtained from ambient pressure to 25 GPa using the third-order Birch-Murnaghan equation of state (BM-EoS) [42, 43]:

$$P(V) = \frac{3B_0}{2} \left[\left(\frac{V_0}{V} \right)^{7/3} - \left(\frac{V_0}{V} \right)^{5/3} \right] \times \left\{ 1 + \frac{3}{4} (B'_0 - 4) \left[\left(\frac{V_0}{V} \right)^{2/3} - 1 \right] \right\} \quad (1)$$

where B'_0 is the first-order pressure derivative of B_0 , V_0 is the unit cell volume at ambient pressure, and V is the unit cell volume at any pressure. The data fitted to the model is illustrated in Figure 4(a), while the obtained EoS parameters for various phases are detailed in Table III. Specifically, the bulk modulus (B_0) for the cubic phase is determined as 202(2) GPa, and for the tetragonal phase, it is 235(6) GPa. In the orthorhombic phase with the Fddd space group, the bulk modulus is 217(2) GPa, and for the Cmc21 space group of the orthorhombic phase, it is 230(2) GPa. Notably, our findings indicate almost similar bulk compressibility in the HP post-spinel phases. The obtained bulk modulus of CTO-Sp in both the spinel and post-spinel phases is comparable to that of similar oxide spinels in their ambient and high-pressure polymorphs [44].

We will now focus on the bulk moduli of various octahedra within different phases of CTO-Sp. Using a third-order Birch-Murnaghan equation of state (BM-EoS), we have fitted the pressure-dependent change in polyhedral volume data, ranging from ambient pressure to 25 GPa. This approach allows us to obtain the polyhedral bulk moduli for different phases, and the corresponding fitted data are depicted in Figures 4(b) and (c). The values for the polyhedral bulk moduli and their pressure derivatives are summarized in Table III. In the cubic phase, the tetrahedral bulk modulus (B_0)_{tet} and the octahedral bulk modulus (B_0)_{oct} are determined as 204(2) GPa and 202(1) GPa, respectively. It is noteworthy

that the compressibility of the two distinct octahedra in the cubic phase is almost identical. The average value of these polyhedral bulk moduli ($\overline{B_0} = 203(3)$ GPa) is nearly the same as the macroscopic bulk modulus ($B_0 = 202(2)$) of CTO-Sp in the cubic phase (refer to Table III). Moving to the tetragonal phase, the tetrahedral and octahedral bulk moduli are found to be 260(1) GPa and 236(7) GPa, respectively. Remarkably, the tetrahedra in the tetragonal phase exhibit lower compressibility compared to the octahedra. The compression and distortion of the tetrahedral unit cell are predominantly achieved through the deformation of the octahedra within the unit cell. The average bulk modulus of these two octahedra ($\overline{B_0}$) is 248(8) GPa, nearly in line (within the error limits) with the bulk modulus ($B_0 = 235(6)$ GPa) of CTO-Sp in the tetragonal phase. For the orthorhombic-Fddd space group, the BM-EoS fit reveals a tetrahedral bulk modulus of approximately 222(1) GPa and an octahedral bulk modulus of around 206(4) GPa. Once again, the octahedra in the Fddd-orthorhombic phase exhibit greater compressibility compared to the tetrahedra. In the case of the Cmc space group, the structure comprises a herringbone octahedra array, as discussed previously. The bulk modulus of $Co^{2+}O_6$ octahedra is estimated to be around 232(2) GPa, while for the $Co^{2+}/Ti^{4+}O_6$ octahedra, it is approximately 231(4) GPa. For both the space groups in the orthorhombic phase, the average polyhedral bulk modulus is comparable with the macroscopic bulk modulus of the respective space groups (see Table III). Therefore, the bulk compressibility of inverse spinel Co_2TiO_4 and its HP post-spinel phases can be estimated as the average polyhedral compressibility within each phase. Recio et al. observed that the bulk compressibility in the direct and inverse spinel-type compounds can be expressed by considering cation oxide polyhedral compressibility along with a term accounting for the hydrostatic pressure effect on the oxygen position in the unit cell [44]. Their theoretical studies indicate that, for many spinel-type compounds, the macroscopic bulk modulus can be estimated as the average of polyhedral bulk moduli [44].

The variability in compressibility across different polyhedra prompts an investigation into the pressure-dependent changes in bond angle variation and distortion indices (bond length) for various polyhedra. The bond angle variance (σ^2) and the distortion index (DI) of the polyhedra can be defined as follows [45]:

$$\sigma^2 = 1/(N - 1) \sum_{i=1}^N (\theta_i - \theta_0)^2 \quad (2)$$

Here, N represents the number of bond angles in the polyhedron, θ_i is the i -th bond angle,

and θ_0 is the ideal bond angle for a regular polyhedron.

$$DI = 1/N \sum_{i=1}^N (|l_i - l_{av}|)/l_{av} \quad (3)$$

In this equation, l_i denotes the distance from the central ion to the i -th coordinating ion, and l_{av} is the average bond length.

In Figure 6(a), it is evident that the tetrahedral bond angle variance is zero in the cubic phase and begins to increase in the tetragonal phase. This increase in bond angle variance is directly associated with the tetrahedral distortion within the system. The escalating bond angle variance signifies a heightened tetrahedral distortion attributed to the Jahn-Teller effect. Thus, the transition from cubic to tetragonal phase is instigated by the tetrahedral distortion due to the Jahn-Teller effect of Co^{2+} cation at the tetrahedral site. Concerning the octahedral distortion, the index remains zero up to around 7 GPa. Beyond this pressure, in the tetragonal phase, it reaches a maximum value of 9.1×10^{-4} , followed by a minimum at about 10.4 GPa, as depicted in Figure 6(b). Above 10.4 GPa, the octahedral distortion index sharply increases, leading to tetragonal to orthorhombic structural phase transition at around 17.3 GPa. The deformation of the octahedra within the tetragonal unit cell is responsible for the increase in tetragonality and distortion of the unit cell. In the orthorhombic phase within the Fddd space group, the distortion index of the octahedra decreases with pressure up to 20.2 GPa, followed by a rapid increase beyond this pressure. This increase in octahedral distortion indicates instability in the Fddd-orthorhombic phase at HP. For the octahedra in the Cmc m -orthorhombic phase, the distortion index of the $Co^{2+}O_6$ octahedra increases up to 20.2 GPa, followed by saturation beyond that pressure, as shown in Figure 6(c). The distortion index of $Co^{2+}/Ti^{4+}O_6$ octahedra in the Cmc m -orthorhombic phase decreases with pressure up to the highest pressure value. The saturation of the distortion index for $Co^{2+}O_6$ octahedra and a decreasing trend in the distortion index for $Co^{2+}/Ti^{4+}O_6$ octahedra imply a rise in the phase fraction percentage along with the stability of the Cmc m -orthorhombic phase at the higher pressures.

B. High-pressure Raman study

As a complementary study to XRD and also to probe the phonon dynamics and the pressure effect on phonon modes, we have performed high-pressure Raman spectroscopy

measurements at ambient temperatures on the inverse spinel polycrystalline Co_2TiO_4 . In the literature, as far as our knowledge, there have not been any systematic HP Raman measurements on CTO-Sp. At ambient conditions, CTO-Sp crystallizes in cubic phase with the space group $Fd\bar{3}m$ (no. 227, $Z = 8$). Hence, according to the group theory analysis, the vibrational modes of CTO-Sp at Γ point are as follows: $\Gamma = A_{1g} + E_g + 3A_{2u} + 3E_u + 3T_{2u} + 3T_{2g} + 7T_{1u} + T_{1g}$. Among which five modes, $(A_{1g} + E_g + 3T_{2g})$ are Raman active. At ambient, we have observed four phonon modes in the Raman spectrum of CTO-Sp, as indicated in Figure 7(a). Two weak phonon modes centered at 174 cm^{-1} and 309.4 cm^{-1} can be identified as $T_{2g}(1)$ and E_g modes respectively. The translational movement of the entire CoO_4 tetrahedron accounts for the mode centred at 174 cm^{-1} ($T_{2g}(1)$). The phonon mode E_g at 309.4 cm^{-1} corresponds to the symmetric bending of oxygen ions with respect to cations in a tetrahedral (CoO_4) environment. The asymmetric bending and stretching of oxygen anion in the Co/TiO_6 octahedra cause a broad peak centered at 531.6 cm^{-1} ($T_{2g}(2)$). The robust and intense peak centered at 701.8 cm^{-1} corresponds to the symmetric stretching of oxygen atoms in the CoO_4 tetrahedra and can be considered A_{1g} symmetry. This A_{1g} mode is often referred to as the tetrahedral breathing mode of spinels. These Raman modes are all assigned following the reported literature by Prosnikov et al. and others [46–48].

We will now examine the impact of external pressure on the phonon modes of polycrystalline CTO-Sp. Figure 7(b) illustrates the pressure-dependent Raman spectrum at selected pressure values. All Raman modes shift to higher energies with increasing pressure. Notably, a new Raman peak (M1) emerges around 18 GPa, as indicated by the red arrows in Figure 7(b). To thoroughly examine the Raman shifts and the variation in linewidth of different modes under pressure, each peak in the Raman spectrum is modeled using a Lorentzian profile, which is well-suited for lifetime-broadened peaks. Baseline correction is not applied to the spectra before fitting, as there are no detectable contributions from fluorescence or continuum signals. The pressure-dependent Raman mode frequencies are plotted in Figure 8(a). The $T_{2g}(1)$ mode, initially centered at 174 cm^{-1} under ambient conditions, exhibits a linear pressure dependency with significant broadening. Beyond 6.5 GPa, this mode is no longer observed. The E_g mode undergoes a slope change around 7 GPa, becoming broader with pressure and disappearing beyond 12 GPa. This behaviour correlates with the structural phase transition from cubic to tetragonal phases, driven by tetrahedral distortion due to the Jahn-Teller effect, as discussed in the HP XRD results. The mode originating from the

Co/TiO_6 octahedra, $T_{2g}(2)$, exhibits a slope change above 17.3 GPa, while the tetrahedral breathing mode, A_{1g} , shows a slight slope at the same pressure. Around 18 GPa, a new peak (M1) is observed at 690 cm^{-1} as indicated in Figure 7(b). The change in slope of $T_{2g}(2)$ and A_{1g} modes and the emergence of the new peak (M1) between 17-18 GPa indicate a structural reorientation of the unit cell of polycrystalline CTO-Sp, corroborated by earlier XRD measurements. A structural transition from tetragonal to orthorhombic phase was observed around 17.3 GPa. Mixed space groups (Fddd + Cmcm) were noted in the HP orthorhombic phase. The newly observed peak possibly originates from the orthorhombic-Cmcm unit cell beyond 17.3 GPa. The presence of A_{1g} tetrahedral breathing mode at higher pressures with minimal slope change across the tetragonal to orthorhombic phase transition indicates a zero distortion index associated with the cation-oxygen bond lengths, as mentioned in the HP XRD study. A triply degenerate mode cannot exist in a tetragonal or orthorhombic structure; it should split. But we observed no splitting of the $T_{2g}(2)$ mode in the tetragonal phase, which could be due to several reasons. The splitting may be very small due to subtle symmetry-lowering effects in the tetragonal phase, making it difficult to resolve experimentally. Additionally, the $T_{2g}(2)$ mode is not sharp, even under ambient conditions. The dynamic disorder could average out local distortions, effectively restoring higher symmetry on the timescale of Raman scattering, thus preventing the expected splitting of the modes. Strong electron-phonon interactions could lead to a renormalization of vibrational modes, masking the splitting that would otherwise occur. Such interactions may be prominent in CTO due to the presence of transition metal ions with partially filled d-orbitals. The $T_{2g}(1)$ mode, which has very low intensity after loading the sample into the diamond anvil cell, makes it challenging to track the splitting. We also refer to studies by Kyono et al. [49] on Fe_2TiO_4 and Wang et al. [47] on Mg_2TiO_4 , which report similar behaviour, where the T_{2g} Raman modes do not show clear splitting in the high-pressure tetragonal and orthorhombic phases, although broadening is observed. Interestingly, the full width at half maximum (FWHM) of the $T_{2g}(2)$ and A_{1g} modes exhibits a minimum at approximately 17 GPa, as illustrated in Figure 8(b). The FWHM of the Raman mode is inversely related to the lifetime of the phonon mode. Increasing pressure gradually introduces strain within the lattice, expected to lead to a reduction in the lifetime of phonons. However, the decrease in phonon-mode FWHM indicates a decrease in anharmonic phonon interactions. A minimum in FWHM of phonon mode suggests a possibility toward strong electron-phonon

interactions, which causes a decrease in the lifetime of phonons after an electronic transition [50–52]. The Gruneisen parameter is widely recognized for its pivotal role in understanding heat capacities and vibrational entropies using the Kieffer model [53, 54]. By employing the bulk modulus derived from our HP XRD data and using the pressure derivative of a vibrational frequency, the Gruneisen parameter (γ) can be determined through the equation:

$$\gamma = -(d \ln \omega / d \ln V)_{P=0} = (B_0 / \omega_0) (d \omega / d P)_{P=0} \quad (4)$$

Here, ω_0 and ω represent the Raman frequency under ambient and HP conditions, respectively. B_0 stands for the bulk modulus specific to a particular phase. The Gruneisen parameters (γ) for the cubic and HP tetragonal phases fall within the range of 0.82-1.07 and 1.07-1.24, respectively. Additionally, the Gruneisen parameters (γ) for the HP orthorhombic Fddd and Cmcm phases vary between 0.12-1.08 and 0.11-1.09, respectively, as detailed in Table IV, and V.

Moreno et al. reported that the post-spinel orthorhombic structure of $CaTi_2O_4$ in the Cmcm space group exhibits 18-24 Raman-active modes at higher pressures [55]. As mentioned in our HP XRD study, the proportion of the Cmcm space group increases with pressure, reaching its maximum at the highest pressure level. Therefore, we expect the occurrence of phonon modes associated with the Cmcm-orthorhombic phase at higher pressures in the Raman spectrum. However, in our HP Raman study, no Raman modes were observed beyond 23 GPa, as previously discussed, even though the XRD peaks remain strong. This absence of phonon modes, along with the minimum in FWHM, provides strong evidence for the metallization of the sample under HP conditions.

To further investigate this, we performed DFT analysis to examine the pressure-dependent metallization of the system. Our calculations employed a similar magnetic configuration for the ambient pressure structure as described by Ghosh et al.[10]. The three phases [cubic, tetragonal, and orthorhombic (Fddd)] exhibit antiferromagnetic ordering with Co atoms in the tetrahedra and octahedra contributing to up-spin and down-spin states, respectively. In each phase, the Co^{2+} ions having three unpaired electrons occupy both tetrahedral and octahedral sites with a high-spin configuration[10]. These unpaired electrons contribute to a total magnetic moment of $3 \mu_B$. Our calculations yield the following magnetic moments per Co site for the phase: (a) cubic ($Fd\bar{3}m$): $\mu_{tet} = 2.696 \mu_B$ and $\mu_{oct} = -2.685 \mu_B$, (b) the tetragonal ($I4_1/amd$): $\mu_{tet} = 2.664 \mu_B$ and $\mu_{oct} = -2.681 \mu_B$, and (c) orthorhombic (Fddd):

$\mu_{tet} = 2.649 \mu_B$ and $\mu_{oct} = -2.672 \mu_B$. These results are in good agreement with previous theoretical studies [10]. Notably, the other orthorhombic (Cmcm) phase exhibits a net ferrimagnetic ground state with Co magnetic moments $\mu_{tet} = 2.649 \mu_B$ and $\mu_{oct} = -0.592 \mu_B$. Our calculations reveal that the Co^{2+} ions at the octahedral sites undergo a high-spin to low-spin transition in the Cmcm-orthorhombic phase. This transition at the octahedral sites is directly linked to the unit cell and octahedral volume collapse at the Cmcm-orthorhombic phase boundary. Figure 9 shows the density of states (DOS) for the four phases in their antiferromagnetic/ferrimagnetic configurations. It has been found that in the cubic (Fd $\bar{3}$ m), tetragonal (I4 $_1$ /amd), and orthorhombic (Fddd) phases, the energy gap is close to 0.53 eV, 0.43 eV, and 0.28 eV, respectively, whereas the orthorhombic (Cmcm) phase exhibits a metallic character.

Typically, binary and ternary transition metal oxides exhibit insulating behaviour under ambient pressure and temperature conditions [11, 56–58]. This insulating nature arises from strong electronic correlation phenomena inherent in the d-bands, classifying them as Mott insulators [59]. Mott insulators are characterized by substantial optical d-d gaps, denoted as U, which separate the upper empty d-band from the lower filled one (Mott-Hubbard gap). Alternatively, they can be characterized by a p-d gap, represented by Δ , which separates the upper p-band from the filled d-band (charge-transfer gap). At ambient conditions, Mott insulators often display large magnetic moments, transitioning into an antiferromagnetic state below the Neel temperature (T_N). The introduction of chemical doping or the application of pressure to Mott insulators has the potential to close the Mott-Hubbard or charge-transfer gap. This process disrupts the Mott-Hubbard d-d correlation, leading to an Insulator-to-Metal Transition (IMT) accompanied by a collapse of the magnetic moment—a phenomenon known as the Mott transition [60]. It is evident that in Mott insulators, a significant volume reduction during a structural transition must be attributed to the occurrence of the Mott transition [17, 61, 62]. In an extensive HP investigation of $\text{Zn}_{0.2}\text{Mg}_{0.8}\text{Fe}_2\text{O}_4$, Rahman et al. [11] observed a substantial 7.5% change in the unit cell volume during the cubic to orthorhombic phase transition. Concurrently, Raman modes vanished at higher pressure, leading them to propose a Mott Insulator-to-Metal Transition (IMT) around 21 GPa. Pasternak et al. [60] reported a first-order IMT induced by pressure in the Mott insulator Fe_2O_3 , characterized by the breakdown of d-d correlation and a collapse of magnetism. Greenberg et al. [62] observed a Mott transition in CaFe_2O_4 around 50 GPa, associated

with an isostructural transition and a sharp 12% decrease in Fe polyhedral volume due to the closure of the Hubbard gap. This transition was accompanied by a high-spin to low-spin transition, leading to the disappearance of most Raman modes and the persistence of a few low-intensity modes. In a recent theoretical study, Leonov et al. [63] identified a pressure-induced Mott insulator-to-metal transition in CoO, MnO, FeO, and NiO. This transition was marked by the simultaneous collapse of local magnetic moments and lattice volume, achieved through a high-spin to low-spin crossover and band-gap closure driven by a change in crystal structure. They also propose the occurrence of quantum critical charge and spin fluctuations near the pressure-driven Mott IMT in correlated systems with spin-state active ions. Consequently, high pressure not only alters crystal symmetry but also induces Mott transition breakdown, coupled with a spin crossover from high-spin to low-spin, leading to the collapse of local magnetic moments and volume reduction. These phenomena are common in many other cobaltites and ferrites, all demonstrating pressure-driven structural phase transitions characterized by the contraction of metal-oxygen polyhedra and a significant reduction in unit cell volume at the transition.

In our HP XRD investigation, a structural transition is observed at approximately 17.3 GPa, shifting from a tetragonal phase to an orthorhombic phase with a mixed space group of Fddd and Cmc_m. During the tetragonal to Cmc_m-orthorhombic phase transition, a pronounced reduction in unit cell volume of approximately 17.5% is noted at the transition pressure, indicating a first-order phase transition with a significant collapse in volume. Additionally, the volume of *Co/TiO₆* octahedra experienced a collapse of around 16% at the phase transition point (refer to Figure 4(c)). Our DFT calculations reveal that Co ions at the octahedral sites undergo a high-spin to low-spin transition in the high-pressure Cmc_m-orthorhombic phase, which also exhibits metallic behaviour. We also observed an increase in the distortion index (DI) of *Co/TiO₆* octahedra at the phase boundary (see Figure 6(b), (c)). This pressure-induced rise in DI results in an increase in the crystal field, contributing to a substantial decrease in the magnetic moment of the metal ions in the B site [11]. As previously discussed, the observed minimum in the FWHM of the *T_{2g}(2)* and *A_{1g}* Raman modes suggests a possible electronic transition near 17.3 GPa. This transition is likely attributed to the pressure-induced closure of the charge-transfer gap, resulting in metallization accompanied by a magnetic collapse. The significant reductions in the unit cell and octahedral volume, along with a high-spin to low-spin transition associated with a spin crossover,

breakdown the Mott-Hubbard d-d correlation, leading to the metallic behaviour of CTO-Sp above 17.3 GPa, accompanied by the collapse of local magnetic moments. A possible electronic transition due to the pressure induces bandgap closer, the absence of all Raman modes, combined with the non-appearance of Raman modes responsible for the Cmc m -orthorhombic phase at HP further supports the notion of a pressure-induced metallization in our sample.

V. CONCLUSION

We have investigated the pressure-induced structural, vibrational and electronic properties, as well as possible magnetic transition, in the inverse spinel Co_2TiO_4 using X-ray diffraction, Raman spectroscopy, and first-principles DFT calculations. Our experiments reveal two structural phase transitions. The first transition, occurring around 7.2 GPa, involves a cubic-to-tetragonal transformation. The second phase transition takes place at approximately 17.3 GPa, involving a shift from tetragonal to orthorhombic phase with a mixed space group, Fddd and Cmc m . The tetragonal to Cmc m -orthorhombic phase transition is characterized by a first-order phase transition accompanied by a substantial volume collapse (17.5% for the unit cell volume and 16% for Co/TiO_6 octahedral volume). The proportion of the Cmc m -orthorhombic phase increases with pressure, reaching its peak at the maximum pressure. The macroscopic bulk modulus for the different phases of CTO-Sp can be estimated as the average polyhedral bulk moduli of the respective phases. The significant reductions in unit cell and octahedral volume, coupled with the high-spin to low-spin transition, result in a pressure-induced metallization, leading to the collapse of local magnetic moments in the Cmc m -orthorhombic phase. The emergence of a new peak and changes in the slope of $T_{2g}(2)$ and A_{1g} modes around 17.3 GPa, as observed in Raman spectroscopy, align with structural reorientation, consistent with XRD measurements. The absence of Raman modes, coupled with the non-appearance of modes linked to the Cmc m -orthorhombic phase beyond 23 GPa, and a possible electronic transition due to the pressure-driven closure of the charge-transfer gap, further supports the idea of a pressure-induced metallization in CTO-Sp. Our results suggest that CTO-Sp undergoes a possible Mott IMT accompanied by a possible magnetic transition around 17.3 GPa, which holds significant implications for understanding the quantum criticality of the Mott transition. Further theoretical studies and

experiments on cobaltites are essential to comprehensively characterize the pressure-driven metallization process.

ACKNOWLEDGMENTS

The authors gratefully acknowledge the financial support from the Department of Science and Technology, Government of India, to visit the XPRESS beamline in the ELETTRA Synchrotron light source under the Indo-Italian Executive Programme of Scientific and Technological Cooperation. MS and SC gratefully acknowledge the CSIR, Government of India, for the financial support to carry out the PhD work.

Author Declarations All authors have an equal contribution. All authors reviewed the manuscript.

-
- [1] K. Tomiyasu, J. Fakunaga, and H. Suzuki, *Phys. Rev. B* **70**, 214434 (2004).
 - [2] Y. Yamasaki, S. Miyasaka, Y. Kaneko, J. -P. He, T. Arima, and Y. Tokura, *Phys. Rev. Lett.* **96**, 207204 (2006).
 - [3] L. Rossi, A. Bobel, S. Wiedmann, R. K uchler, Y. Motome, K. Penc, N. Shannon, H. Ueda, and B. Bryant, *Phys. Rev. Lett.* **123**, 027205 (2019).
 - [4] Y. J. Choi, J. Okamoto, D. J. Huang, K. S. Chao, H. J. Lin, C. T. Chen, M. van Veenendaal, T. A. Kaplan, and S-W. Cheong, *Phys. Rev. Lett.* **102**, 067601 (2009).
 - [5] T. Suzuki and T. Katsufuji, *Phys. Rev. B* **77**, 220402(R) (2008).
 - [6] R. E. Camley, Z. Celinski, T. Fal, A. V. Glushchenko, A. J. Hutchison, Y. Khivintsev, B. Kuanr, I. R. Harward, V. Veerakumar, and V. V. Zagorodnii, *J. Magn. Magn. Mater.* **321**, 2048 (2009).
 - [7] Y. Naito and K. Suetake, *IEEE Trans. Microw. Theory Tech.* **19**, 65 (1971).
 - [8] V. G. Harris, A. Geiler, Y. Chen, S. D. Yoon, M. Wu, A. Yang, Z. Chen, P. He, P. V. Parimi, X. Zuo, C. E. Patton, M. Abe, O. Acher, and C. Vittoria, *J. Magn. Magn. Mater.* **321**, 2035 (2009).
 - [9] R. L. Millard, R. C. Peterson, and B. K. Hunter, *Am. Miner.* **80**, 885 (1995).

- [10] S. Ghosh, S. Singh, D. C. Joshi, P. Pramanik, S. Ghosh, P. K. Mishra, and S. Thota, *Phys. Rev. B* **98**, 235119 (2018).
- [11] S. Rahman, S. Samanta, D. Errandonea, S. Yan, K. Yang, J. Lu, and L. Wang, *Phys. Rev. B* **95**, 024107 (2017).
- [12] B. S. Boyanov, *J. Thermal Anal.* **41**, 1607 (1994).
- [13] G. Subías, V. Cuartero, J. García, J. Blasco, S. Lafuerza, S. Pascarelli, O. Mathon, C. Strohm, K. Nagai, M. Mito, and G. Garbarino, *Phys. Rev. B* **87**, 094408 (2013).
- [14] G. Kh. Rozenberg, Y. Amiel, W. M. Xu, M. P. Pasternak, R. Jeanloz, M. Hanfland, and R. D. Taylor, *Phys. Rev. B* **75**, 020102(R) (2007).
- [15] H. Suzuki, T. Furubayashi, G. Cao, H. Kitazawa, A. Kamimura, K. Hirata, and T. Matsumoto, *J. Phys. Soc. Jpn.* **68**, 2495 (1999).
- [16] M. Francisco Javier, *Pressure-Induced Phase Transitions in AB₂X₄ Chalcogenide Compounds* (Springer, Berlin, 2014).
- [17] R. Arielly, W. M. Xu, E. Greenberg, G. K. Rozenberg, M. P. Pasternak, G. Garbarino, S. Clark, and R. Jeanloz, *Phys. Rev. B* **84**, 094109 (2011).
- [18] S. Sent, W. Blum, and H. Hesse, *Philos. Mag. A* **81**, 109 (2001).
- [19] R. L. Millard, R. C. Peterson, and B. K. Hunter, *Am. Miner.* **80**, 885 (1995).
- [20] S. -H. Shim, T. S. Duffy, and G. Shen, *Nature (London)* **411**, 571(2001).
- [21] H. S. C. O'neil and A. Navrotsky, *Am. Miner.* **69**, 733 (1984).
- [22] S. Moorbath, H. Welke, and N. H. Gale, *Earth Planet. Sci. Lett.* **6**, 245 (1969).
- [23] S. Nayak, S. Thota, D. C. Joshi, M. Krautz, A. Waske, A. Behler, J. Eckert, T. Sarkar, M. S. Andersson, R. Mathieu, V. Narang, and M. S. Seehra, *Phys. Rev. B* **92**, 214434 (2015).
- [24] A. Wei, S. Tao, Y. Fang, Z. D. Han, B. Qian, X. F. Jiang, H. Zhou, R. J. Tang, D. H. Wang, *J. Magn. Magn. Mater.* **441**, 361 (2017).
- [25] S. Nayak, D. C. Joshi, M. Krautz, A. Waske, J. Eckert, and S. Thota, *J. Appl. Phys.* **119**, 043901 (2016).
- [26] S. Nayak, K. Dasari, D. C. Joshi, P. Pramanik, R. Palai, A. Waske, R. N. Chauhan, N. Tiwari, T. Sarkar, and S. Thota, *J. Appl. Phys.* **120**, 163905 (2016).
- [27] G. Gavaille, J. Hubsch, and S. Koutani, *J. Magn. Magn. Mater.* **102**, 283 (1991).
- [28] Z. Wang, S. K. Saxena, and C. S. Zha, *Phys. Rev. B* **66**, 024103 (2002).
- [29] T. Yamanaka, T. Mine, S. Asogawa, and Y. Nakamoto, *Phys. Rev. B* **80**, 134120 (2009).

- [30] Y. Zhang, X. Liu, S. R. Shieh, Z. Zhang, X. Bao, T. Xie, F. Wang, C. Prescher, and V. B. Prakapenka, *Phys. Chem. Miner.* **46**, 571 (2019).
- [31] Q. -Y. Liu, H. Wang, X. Liu, L. Tao, J. Liu, D. Chen, K. Sun, Z. Liu, J. Cheng, M. Huo, X. Wang, and Y. Sui, *Phys. Rev. B* **104**, 064407 (2021).
- [32] J. Hubsch and G. Gavoille, *Phys. Rev. B* **26**, 3815 (1982).
- [33] C. Prescher and V. B. Prakapenka, *High Press. Res.* **35**, 223 (2015).
- [34] R. Shirley, *The CRYSFIRE System for Automatic Powder Indexing: User's Manual* (The Lattice Press, Guildford, UK,1999).
- [35] B. H. Toby, *J. Appl. Crystallogr.* **34**, 210 (2001).
- [36] H. Mao, J.-A. Xu, and P. Bell, *J. Geophys. Res.* **91**, 4673 (1986).
- [37] G. Kresse and J. Furthmüller, *Phys. Rev. B* **54**, 11169 (1996).
- [38] J. P. Perdew, K. Burke, and M. Ernzerhof, *Phys. Rev. Lett.* **77**, 3865 (1996).
- [39] P. E. Blöchl, *Phys. Rev. B* **50**, 17953 (1994).
- [40] S. Klotz, J. -C. Chervin, P. Munsch, and G. L Marchand, *J. Phys. D: Appl. Phys.* **42**, 075413 (2009).
- [41] X. Chen, H. Lou, Z. Zeng, B. Cheng, X. Zhang, Y. Liu, D. Xu, K. Yang, and Q. Zeng, *Matter Radiat. Extremes* **6**, 038402 (2021).
- [42] F. Birch, *Phys. Rev.* **71**, 809 (1947).
- [43] R. J. Angel, M. Alvaro, and J. G.-Platas, *Z. Kristallogr. Cryst. Mater.* **229**, 405 (2014).
- [44] J. M. Recio, R. Franco, A. Martín Pendás, M. A. Blanco, L. Pueyo, and R. Pandey, *Phys. Rev. B* **63**, 184101 (2001).
- [45] K. Momma and F. Izumi, *VESTA: a Three-Dimensional Visualization System for Electronic and Structural Analysis: Manual* (2019).
- [46] M. A. Prosnikov, A. D. Molchanova, R. M. Dubrovin, K. N. Boldyrev, A. N. Smirnov, V. Y. Davydov, A. M. Balbashov, M. N. Popova, and R. V. Pisarev, *Phys. Solid State* **58**, 2516 (2016).
- [47] C. P. Wang, S. R. Shieh, A. C. Withers, X. Liu, D. Zhang, S. N. Tkachev, A. E. Djirar, T. Xie, and J. D. Rumney, *Sci. Rep.* **10**, 6278 (2020).
- [48] S. Nayak, K. Dasari, D. C. Joshi, P. Pramanik, R. Palai, V. Sathe, R. N. Chauhan, N. Tiwari, and S. Thota, *Phys. Status Solidi B* **253**, 2270 (2016).
- [49] A. Kyono, M. Ahart, T. Yamanaka, S. Gramsch, H-k Mao, R. J. Hemley, *Am. Mineral.* **96**,

- 1193 (2011).
- [50] S. N. Gupta, A. Sing, K. Pal, B. Chakraborti, D. V. S. Muthu, U. V. Waghmare, and A. K. Sood, *Phys. Rev. B* **96**, 094104 (2017).
- [51] A. Bera, K. Pal, D. Muthu, S. Sen, P. Guptasarma, U. V. Waghmare, and A. K. Sood, *Phys. Rev. Lett.* **110**, 107401 (2013).
- [52] P. Saha, B. Ghosh, R. Jana, and G. D. Mukherjee, *J. Appl. Phys.* **123**, 204306 (2018).
- [53] S. W Kieffer, *Rev. Geophys.* **17**, 20 (1979).
- [54] S. W Kieffer, *Rev. Geophys.* **17**, 1 (1979).
- [55] S. L. Moreno, P. R. Hernández, A. Muñoz, A. H. Romero, F. J. Manjón, D. Errandonea, E. Rusu, and V. V. Ursaki, *Ann. Phys. (Berlin)* **523**, 157 (2011).
- [56] G. K. Rozenberg, M. P. Pasternak, W. M. Xu, Y. Amiel, M. Hanfland, M. Amboage, R. D. Taylor, and R. Jeanloz, *Phys. Rev. Lett.* **96**, 045705 (2006).
- [57] H. Okada, K. Koyama, M. Hedo, Y. Uwatoko, K. Watanabe, *Physica B* **403**, 1612 (2008).
- [58] T. Furubayashi, T. Kosaka, J. Tang, T. Matsumoto, Y. Kato, and S. Nagata, *J. Phys. Soc. Japan* **66**, 1563 (1997).
- [59] N. F. Mott, *Metal-Insulator Transitions* (Taylor & Francis, London, 1990).
- [60] M. P. Pasternak, G. K. Rozenberg, G. Y. Machavariani, O. Naaman, R. D. Taylor, and R. Jeanloz, *Phys. Rev. Lett.* **82**, 4663 (1999).
- [61] G. K. Rozenberg, L. S. Dubrovinsky, M. P. Pasternak, O. Naaman, T. L. Bihan, and R. Ahuja, *Phys. Rev. B* **65**, 064112 (2002).
- [62] E. Greenberg, G. K. Rozenberg, W. Xu, M. P. Pasternak, C. McCammon, K. Glazyrin, and L. S. Dubrovinsky, *Phys. Rev. B* **88**, 214109 (2013).
- [63] I. Leonov, A. O. Shorikov, V. I. Anisimov, and I. A. Abrikosov, *Phys. Rev. B* **101**, 245144 (2020).

Table I. Rietveld-refined structural parameters for the XRD pattern of CTO-Sp are listed for both the ambient cubic phase and the tetragonal phase at 9.6 GPa. The goodness-of-fit is characterized by $R_{wp} = 4.2\%$, $R_p = 1.6\%$ (for cubic) and $R_{wp} = 4.1\%$, $R_p = 2.2\%$ (for tetragonal)

Cubic ($Fd\bar{3}m$)						Tetragonal ($I4_1/amd$)				
Atoms	Wyck.	Occu.	x/a	y/b	z/c	Wyck.	Occu.	x/a	y/b	z/c
Co1	8b	1	0.3750	0.3750	0.3750	4a	1	0.0000	0.7500	0.1250
Co2	16c	0.5	0.0000	0.0000	0.0000	8c	0.5	0.0000	0.5000	0.5000
Ti	16c	0.5	0.0000	0.0000	0.0000	8c	0.5	0.0000	0.5000	0.5000
O	32e	1	0.2430	0.2430	0.2430	16h	1	0.0000	0.0196	0.2606
a=8.4473(7)Å,						a=5.8845(7)Å,				
V=602.788(13)Å ³						c=8.3374(5)Å				
						V=288.711(1)Å ³				

Table II. Rietveld-refined structural parameters for the XRD pattern of CTO-Sp are listed for both the $Fddd$ and $Cmcm$ space group in the orthorhombic phase at 19.1 GPa. The goodness-of-fit is characterized by $R_{wp} = 3.7\%$ and $R_p = 1.8\%$

Orthorhombic: $Fddd$						Orthorhombic: $Cmcm$					
Atoms	Wyck.	Occu.	x/a	y/b	z/c	Atom	Wyck.	Occu.	x/a	y/b	z/c
Co1	8a	1	0.1250	0.1250	0.1250	Co1	4c	1	0.0000	0.3809	0.2500
Co2	16d	0.5	0.5000	0.5000	0.5000	Co2	8f	0.5	0.0000	0.1331	0.0753
Ti	16d	0.5	0.5000	0.5000	0.5000	Ti	8f	0.5	0.0000	0.1331	0.0753
O	32h	1	0.2610	0.2650	0.2590	O1	4c	1	0.0000	0.0581	0.2500
						O2	8f	1	0.0000	0.2421	0.6028
						O3	4b	1	0.0000	0.5000	0.0000
a=8.2650(2)Å,						a=2.7521(7)Å,					
b=8.3321(7)Å,						b=8.8650(2)Å,					
c=8.1670(6)Å						c=9.5185(8)Å					
V=562.41(6)Å ³						V=232.220(7)Å ³					

Table III. Macroscopic and polyhedral values of B_0 and B'_0 for various phases of CTO-Sp. \bar{B}_0 represents the average polyhedral bulk modulus, as defined in the text. The unit of bulk modulus is GPa.

	Cubic: $Fd\bar{3}m$	Tetragonal: $I4_1/amd$	Orthorhombic: $Fddd$	Orthorhombic: $Cmcm$
B_0	202(2)	235(6)	217(2)	230(2)
B'_0	3.8(0.5)	7(1.5)	2.7(0.1)	3.79(0.3)
$(B_0)_{tet}$	204(2)	260(1)	222(1)	...
$(B'_0)_{tet}$	3.5 (0.6)	6.6(0.3)	0.6(0.05)	...
$(B_0)_{oct}$	202(1)	236(7)	206(4)	231(4)
$(B'_0)_{oct}$	3.8(0.3)	10(1.5)	1.5(0.3)	3.91(0.4)
$(B_0)_{Co^2+O_6}$	232(2)
$(B'_0)_{Co^2+O_6}$	3.8(0.15)
\bar{B}_0	203(3)	248(8)	214(5)	231.5(6)

Table IV. Raman modes, their pressure coefficients $d\omega/dP$, and calculated mode Gruneisen parameters (γ) for the cubic and tetragonal phases of CTO-Sp.

Raman modes ω_0 (cm^{-1})	Cubic: $Fd\bar{3}m$		Tetragonal: $I4_1/amd$	
	$d\omega/dP(\text{cm}^{-1}/\text{GPa})$	γ	$d\omega/dP(\text{cm}^{-1}/\text{GPa})$	γ
174 ($T_{2g}(1)$)	0.74	0.82
309.4 (E_g)	1.37	0.89	1.81	1.24
531.6 ($T_{2g}(2)$)	2.39	0.87	2.39	1.07
701.8 (A_{1g})	3.77	1.07	3.77	1.20

Table V. Raman modes, their pressure coefficients $d\omega/dP$, and calculated mode Gruneisen parameters (γ) for the different space groups of the post-spinel orthorhombic phase of CTO-Sp.

Raman modes ω_0 (cm^{-1})	Orthorhombic: $Fddd$		Orthorhombic: $Cmcm$	
	$d\omega/dP(\text{cm}^{-1}/\text{GPa})$	γ	$d\omega/dP(\text{cm}^{-1}/\text{GPa})$	γ
174 ($T_{2g}(1)$)
309.4 (E_g)
576 ($T_{2g}(2)$)	0.28	0.10	0.28	0.11
764 (A_{1g})	3.09	0.90	3.09	0.90
690 (new mode, M1)	3.32	1.08	3.32	1.09

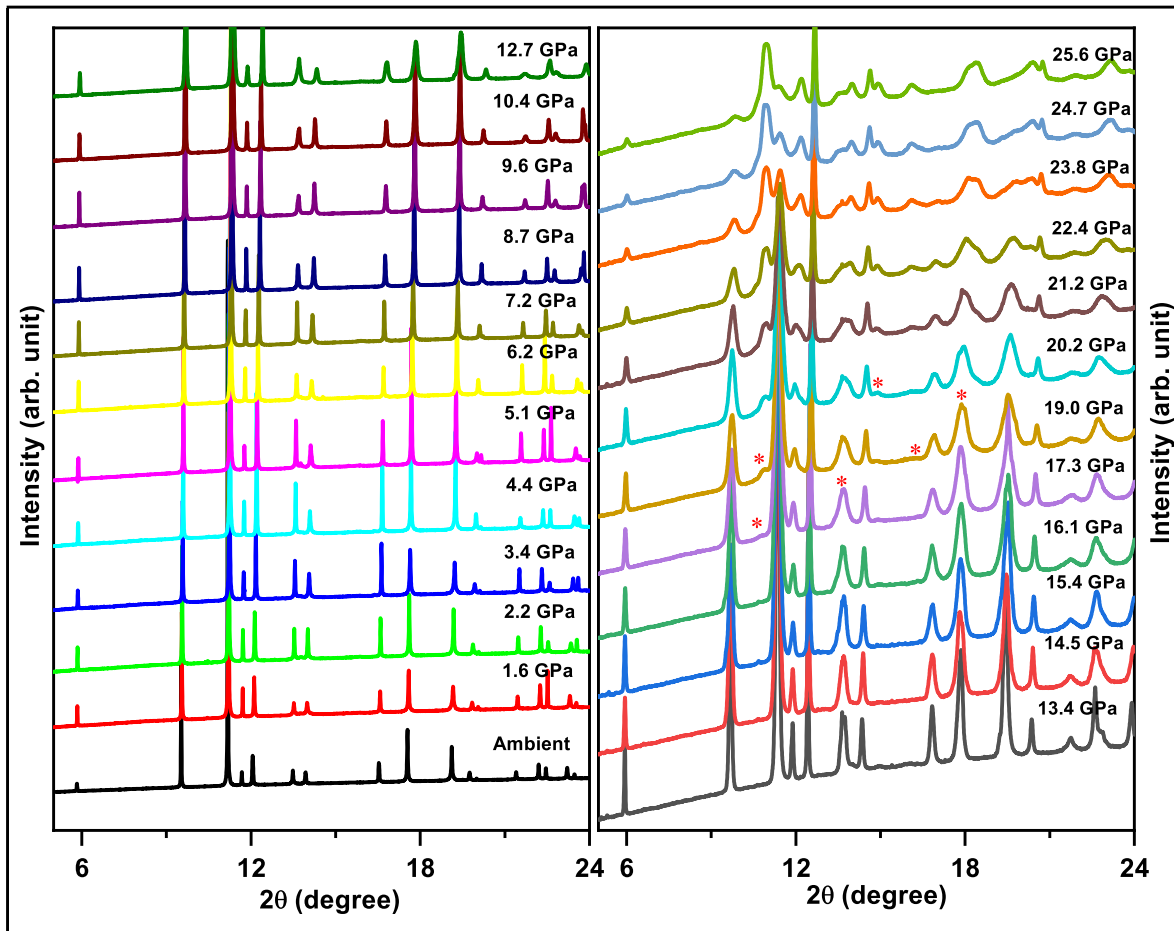


Figure 1. X-ray powder diffraction patterns of C_2TiO_4 at selected pressures.

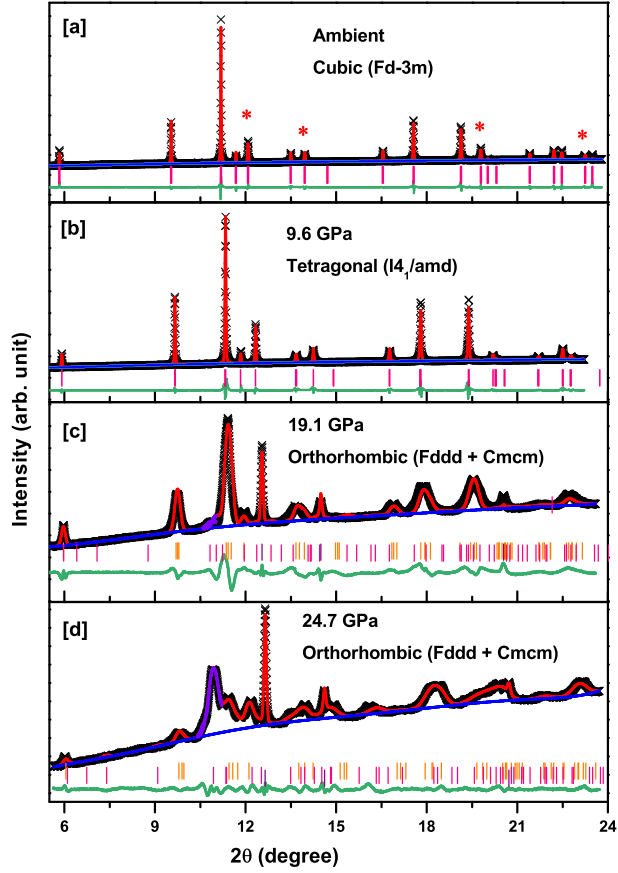


Figure 2. Rietveld refinement of X-ray powder diffraction patterns for Co_2TiO_4 at [a] ambient pressure (cubic phase, space group: $Fd\bar{3}m$) [b] 9.6 GPa (tetragonal phase, space group: $I4_1/amd$) [c] 19.1 GPa, and [d] 24.7 GPa (orthorhombic phase, space groups: $Fddd + Cmc$). The black crosses represent observed data points, while the red and violet lines over the data points depict the fit to the data. The intensity of the peak corresponding to the Cmc space group increases with pressure, as shown by the violet line. The blue line indicates the background, and the difference between observed and fitted data is illustrated by the green line. Bragg positions are marked by vertical bars. In the orthorhombic phase, the orange and pink vertical bars represent the Bragg positions of the $Fddd$ and Cmc space groups, respectively. Diffraction peaks of the pressure marker are indicated by red star markers.

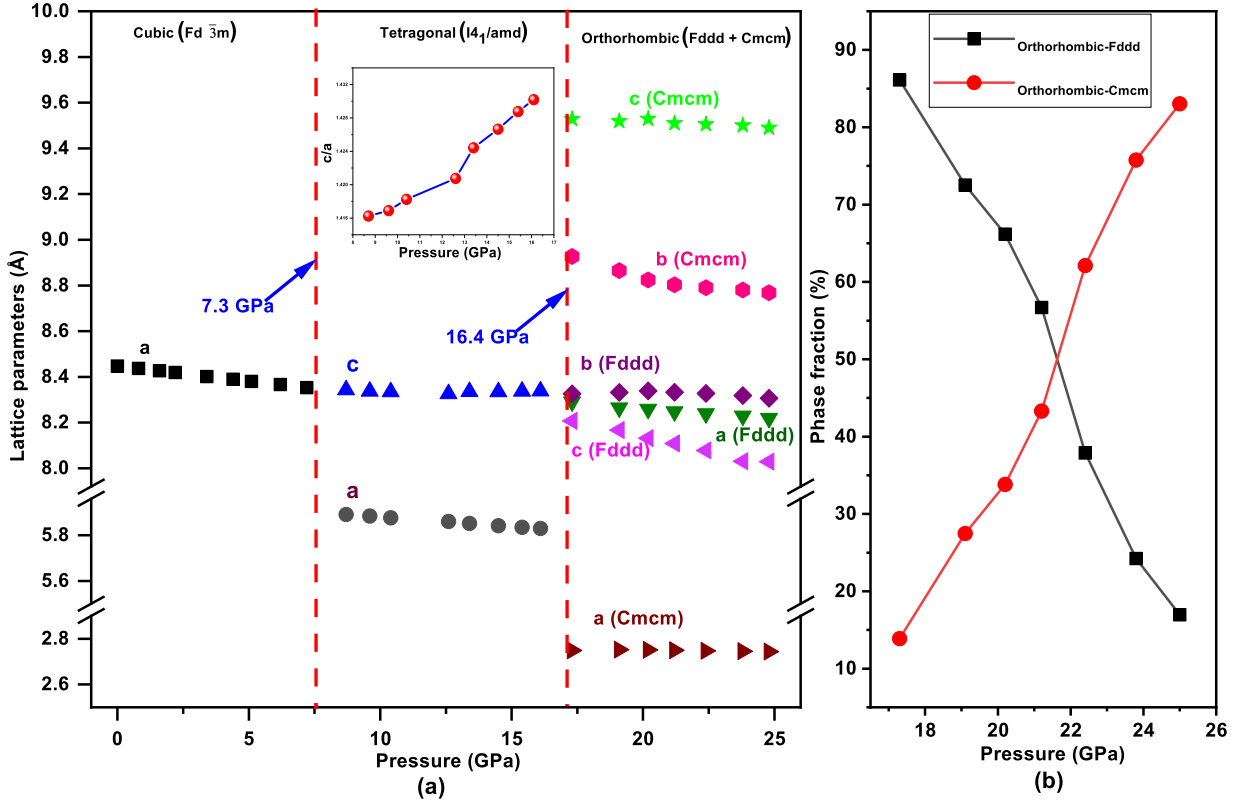


Figure 3. (a) Lattice parameter of the unit cells for the three different phases. In the tetragonal phase of Co_2TiO_4 , the tetragonality (c/a) as a function of pressure is illustrated in the inset. [b] Pressure-dependent phase fraction percentage for the two different space groups in the orthorhombic phase.

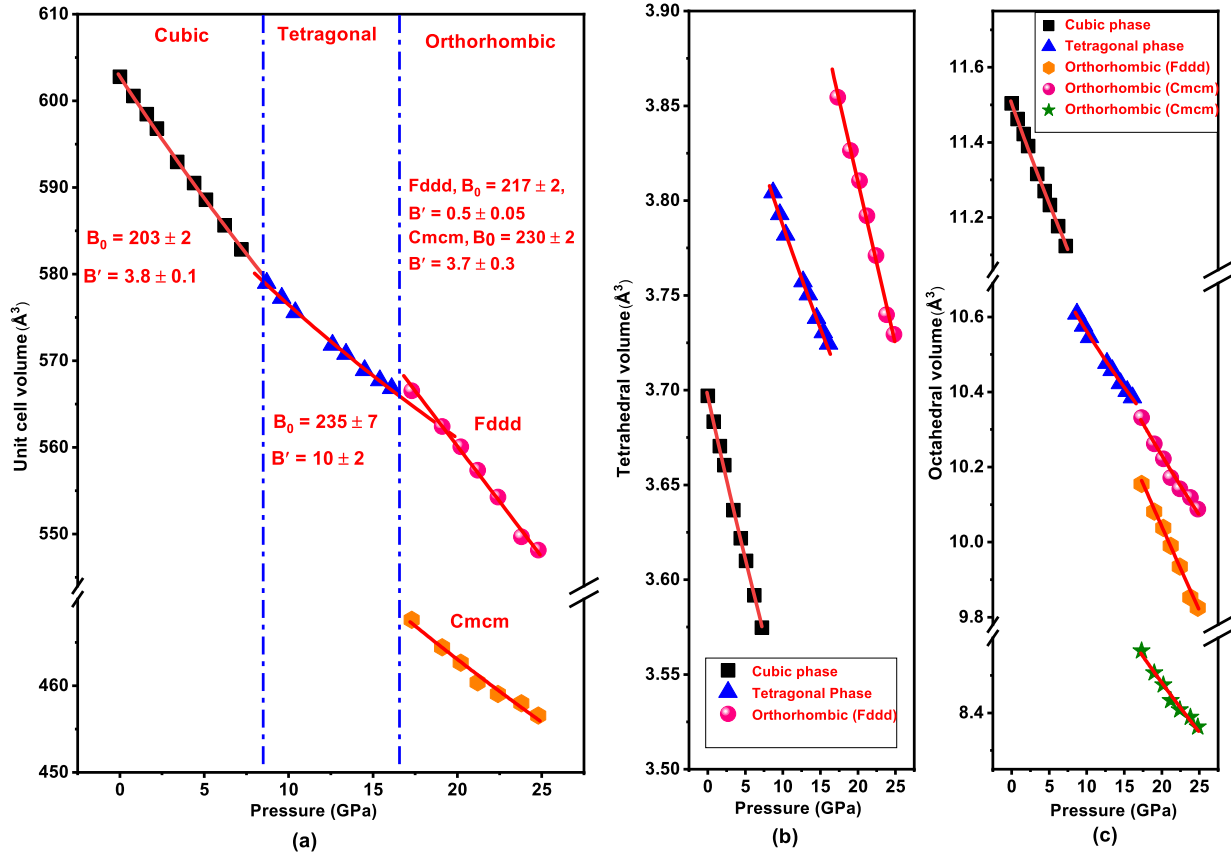


Figure 4. Evolution of pressure: (a) unit cell volume of polycrystalline CTO-Sp across three phases, (b) tetrahedral volume for various phases, (c) octahedral volume for the three phases. Solid lines through the data points represent the fitting using the Birch-Murnaghan equation of state (BM-EoS).

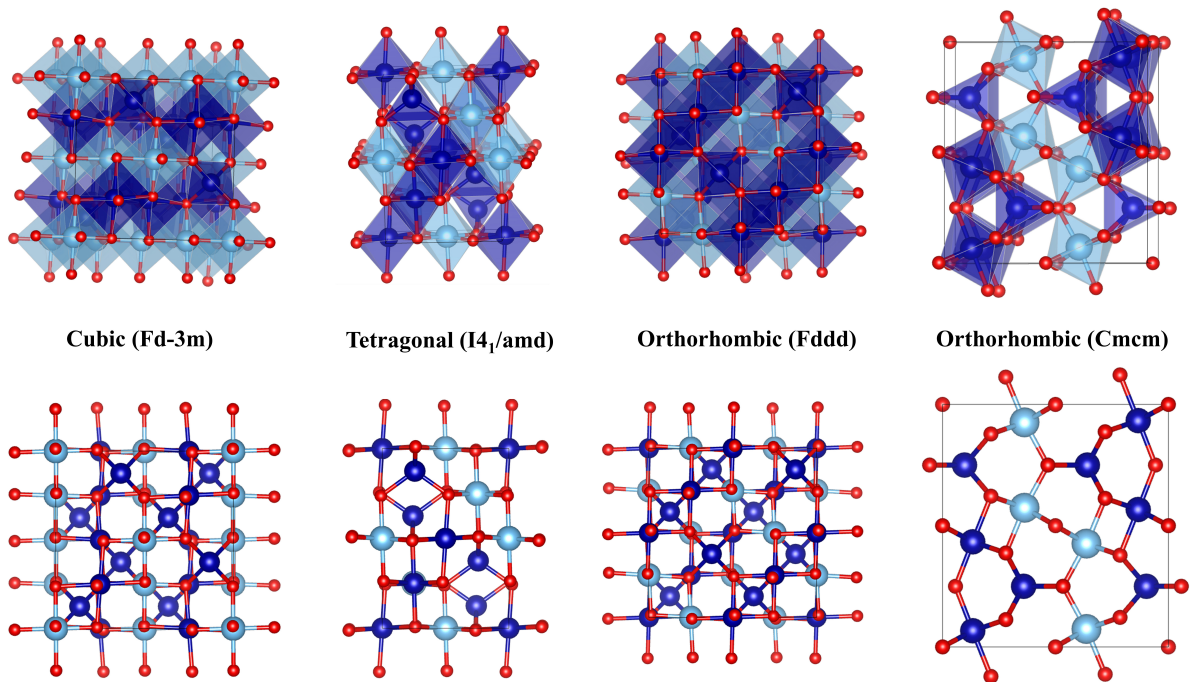


Figure 5. The optimized crystal structures for the different phases. The initial lattice parameters and the atom positions are obtained from our Rietveld refined XRD data.

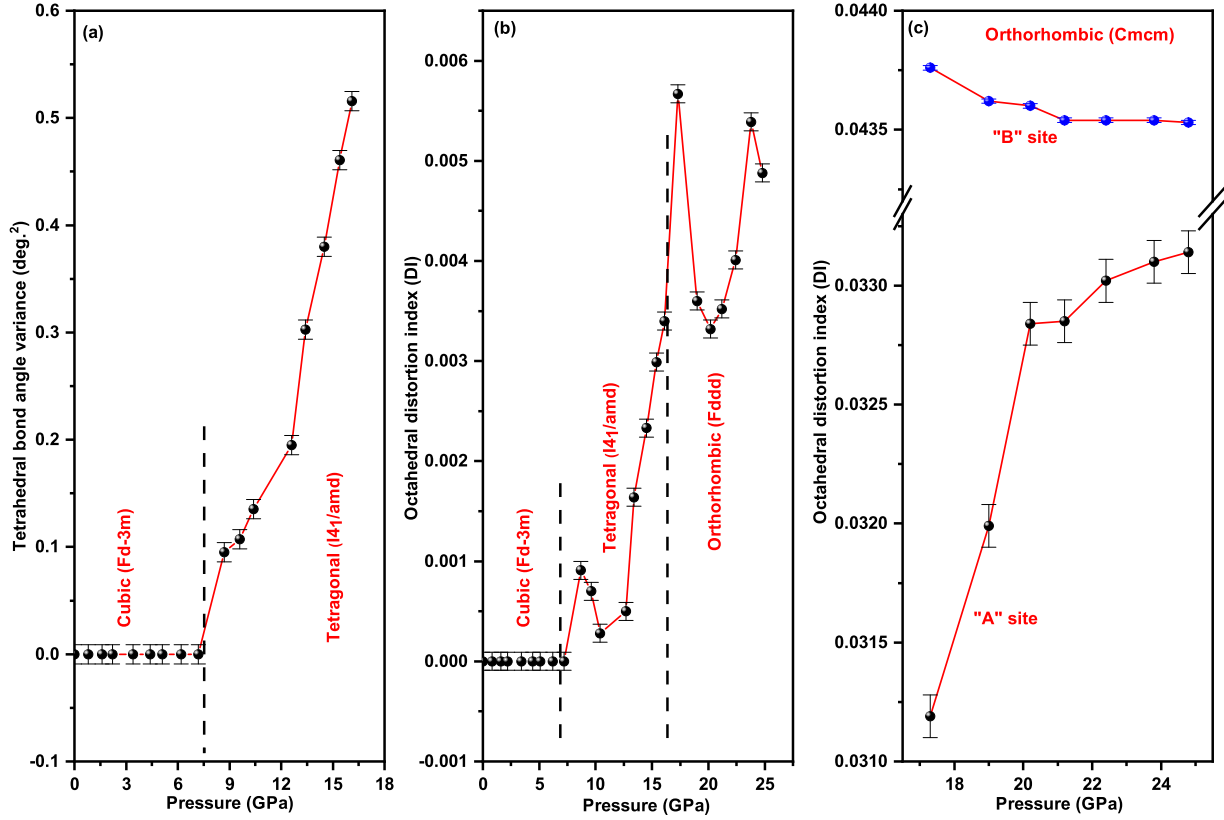
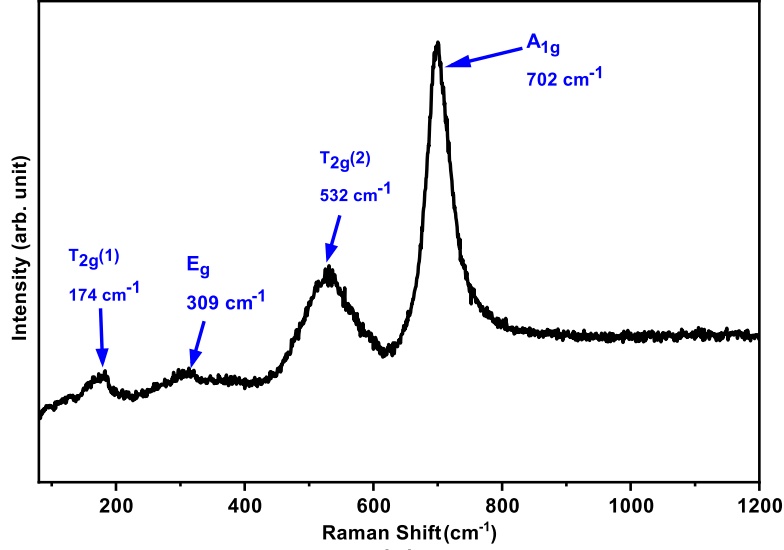
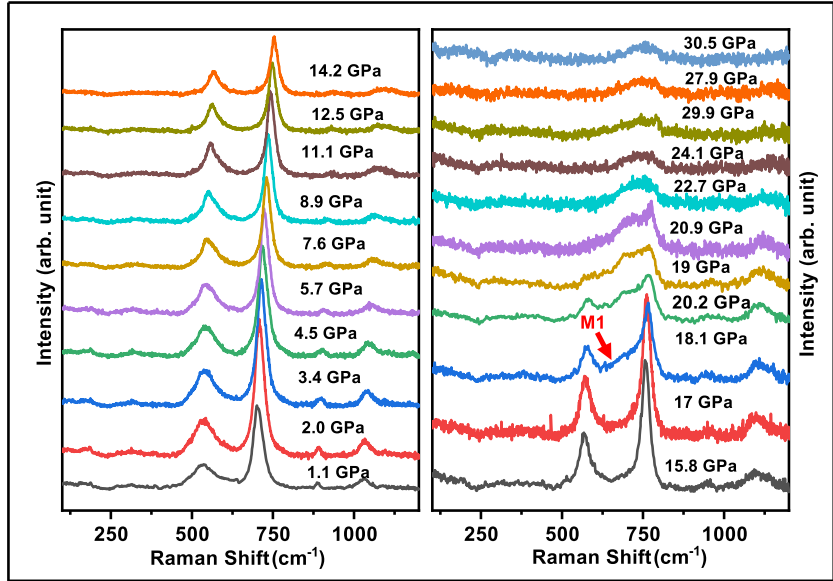


Figure 6. pressure-dependent variations: (a) tetrahedral bond angle variance in both cubic and tetragonal phases, (b) octahedral distortion index (DI) in cubic ($Fd\bar{3}m$), Tetragonal ($I4_1/amd$), and orthorhombic ($Fddd$) phases, and (c) octahedral DI specifically for the orthorhombic-Cmcm phase. Connecting lines between the data points serve as visual guides.



(a)



(b)

Figure 7. (a) Raman spectrum of Co_2TiO_4 at ambient conditions, obtained with a 532 nm laser as the excitation source. All modes are labelled in the figure. (b) Pressure evolution of Raman spectra at selected pressure points. The emergence of a new Raman mode in the orthorhombic phase is indicated by M1.

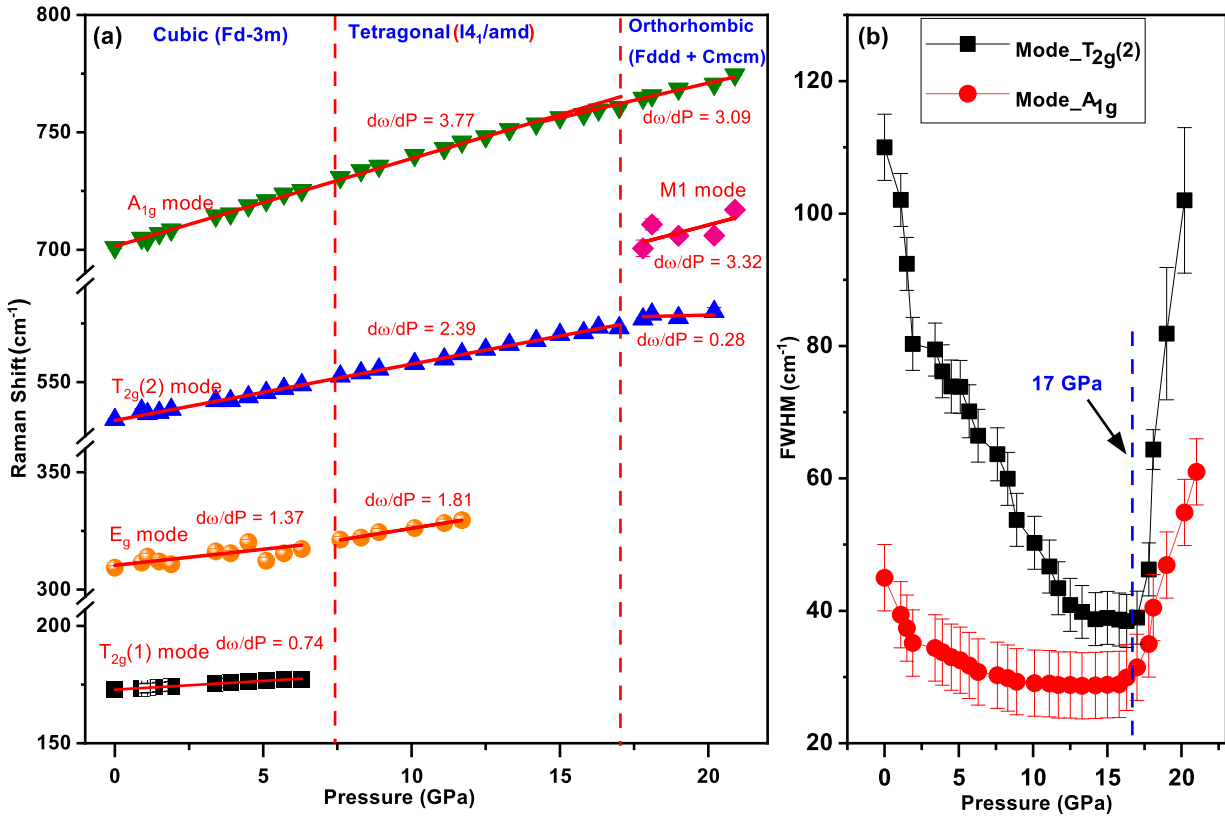


Figure 8. (a) Raman mode values observed in polycrystalline Co_2TiO_4 as a function of pressure. Slope discontinuities along with the disappearance of phonon modes observed at 6.5 GPa and 17.3 GPa. A new mode M1 observed in the HP orthorhombic phase. (b) Pressure-dependent Full Width at Half Maximum (FWHM) of the $T_{2g}(2)$ and A_{1g} modes, revealing a minimum at approximately 17 GPa.

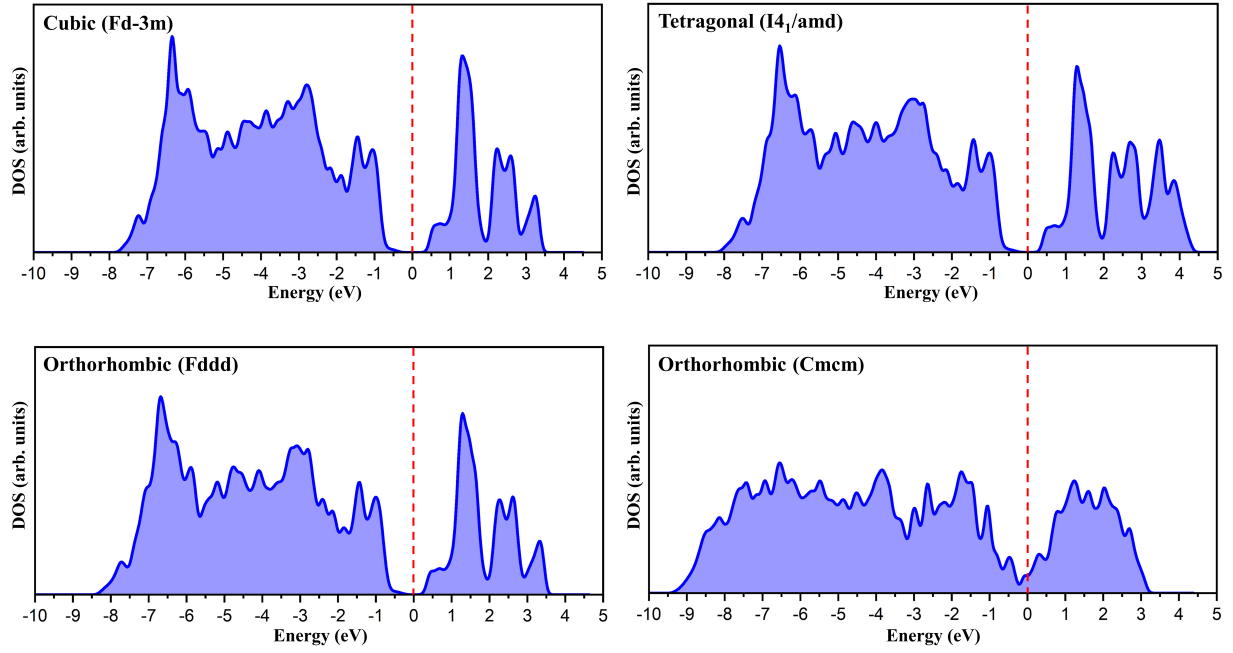


Figure 9. Total electronic density of states for the four different phases in their antiferromagnetic/ferromagnetic configurations with $U_{eff} = 4.0$ eV for Co ions.